

Design and Characterization of a Gradient-Transparent RF Copper Shield for PET Detector Modules in Hybrid MR-PET Imaging

*Original*

Design and Characterization of a Gradient-Transparent RF Copper Shield for PET Detector Modules in Hybrid MR-PET Imaging / Berneking, Arne; Trincherò, Riccardo; Ha, Yonghyun; Finster, Felix; Cerello, Piergiorgio; Lerche, Christoph; Shah, Nadim Jon. - In: IEEE TRANSACTIONS ON NUCLEAR SCIENCE. - ISSN 0018-9499. - 64:5(2017), pp. 1118-1127. [10.1109/TNS.2017.2691546]

*Availability:*

This version is available at: 11583/2716676 since: 2021-03-31T18:36:34Z

*Publisher:*

Institute of Electrical and Electronics Engineers Inc.

*Published*

DOI:10.1109/TNS.2017.2691546

*Terms of use:*

This article is made available under terms and conditions as specified in the corresponding bibliographic description in the repository

*Publisher copyright*

IEEE postprint/Author's Accepted Manuscript

©2017 IEEE. Personal use of this material is permitted. Permission from IEEE must be obtained for all other uses, in any current or future media, including reprinting/republishing this material for advertising or promotional purposes, creating new collecting works, for resale or lists, or reuse of any copyrighted component of this work in other works.

(Article begins on next page)

# Design and Characterization of a Gradient-Transparent RF Copper Shield for PET Detector Modules in Hybrid MR-PET Imaging

Arne Berneking\*, Riccardo Trincheri\*, *Member, IEEE*,  
YongHyun Ha, Felix Finster, Piergiorgio Cerello, Christoph Lerche, N. Jon Shah

**Abstract**—This paper focuses on the design and the characterization of a frequency-selective shield for PET detector modules of hybrid MR-PET scanners where the shielding of the PET cassettes is located close to the observed object. The proposed shielding configuration is designed and optimized to guarantee a high shielding effectiveness of up to 60 dB for  $B_1$ -fields at the Larmor frequency of 64 MHz to prevent interactions between the RF coil and PET electronics. On the other hand, the shield is transparent to the gradient fields with the consequence that eddy current artifacts in the acquired EPI images are significantly reduced with respect to the standard solid-shield configuration. The frequency-selective behavior of the shield is characterized and validated via simulation studies with CST MICROWAVE STUDIO in the MHz and kHz range. Bench measurements with a RF coil built in-house demonstrated the high shielding effectiveness at the Larmor frequency. Moreover, measurements on a 4T human scanner confirmed the abolishment of eddy current artifact also providing an understanding of which surfaces eddy currents flow with respect to the sequence parameters. Simulations and measurements for the proposed shielding concept were compared to a solid copper shielding configuration.

**Index Terms**—RF shielding for PET cassettes, simultaneous MR-PET, hybrid scanner, gradient-transparent, frequency-selective, eddy current reduction, EPI artifacts.

## I. INTRODUCTION

One of the main challenges in hybrid MR-PET scanner design is to prevent interferences between components and parts of the two image modalities. From a magnetic resonance imaging (MRI) perspective, positron emission tomography (PET) components are integrated into the MRI scanner and these perturb the sensitive magnetic fields of the MRI scanner. On the other hand, from the PET standpoint, strong magnetic fields interfere with the PET electronics and can compromise the reliability of the PET data acquisition electronics. While the alteration of the static  $B_0$ -field can be theoretically circumvented by the use of non-magnetic components, interferences with the  $B_1$ -field and the gradient fields,  $G$ , require additional integration methods.

In particular, radio-frequency (RF) coils tuned to the Larmor frequency are used to generate a magnetic field  $B_1$  in the MHz range with an amplitude of  $\mu\text{T}$  perpendicular to  $B_0$  to excite spins from their aligned equilibrium state. Due to the alternating  $B_1$ -field, an electric component cannot be avoided and is also always generated by the RF coils. The field generated by the RF coil with a RF power of up to kW can disturb the PET electronic during the PET data acquisition. Additionally, the sensitive RF coils are able to detect the small nuclear magnetic resonance (NMR) signal, which is in the  $\mu\text{V}$  range. Thus, MRI coils, especially receive coils, are also very noise sensitive and able to pick up noise emitted from the PET electronics.

In early days of simultaneous MR-PET only Cerium Doped Lutetium Oxyorthosilicate (LSO) and Cerium-doped Lutetium Yttrium Orthosilicate (LYSO) scintillator crystals were placed inside the magnetic field and coupled optically to photomultiplier tubes (PMT), which were placed outside the MRI scanner bore [1]. Subsequent use of MRI-compatible solid-state photo sensors [2]–[6] led to increased integration of electronic components inside the scanner bore. Hence, state-of-the-art MR-PET imaging devices can include digitization of acquired PET data inside the scanner bore and integration of application-specific integrated circuits (ASIC) and field-programmable gate array (FPGA) [7]–[9]. Consequently, shielding concepts with high shielding effectiveness (SE) are required to cover the PET-cassette housing including the additional electronics.

Commonly an RF shield is installed between RF coils and PET data acquisition systems [10] to avoid electromagnetic (EM) coupling between the two parts thereby shielding the interior of the cassette from the EM field generated by the RF coils. Generally, the SE is higher for highly conductive materials as e.g., copper, silver and aluminum [11]. However, to avoid MR image disturbances, the shield should not interact with the gradient fields. In fact, rapid switching of current in the gradient coils induces eddy currents in high conductive shields due to the law of induction. Back-induced fields generated by the eddy currents interfere with these image-encoding gradient fields. Consequently, the encoding gradients are changed leading to artifacts in the MR images. This effect is especially critical in MRI sequences such as Echo-planar Imaging (EPI) [12] and EPI with Keyhole (EPIK) [13], which require fast switching gradients, as well in scanners which provide strong gradient systems to improve applications such as diffusion MRI [14].

\* The first two authors contributed equally to this work.

A. Berneking, F. Finster, Y. Ha, C. Lerche, N. J. Shah are with the Medical Imaging Physics Department (INM-4), Institute for Neuroscience and Medicine, Forschungszentrum Jülich GmbH (e-mail: a.berneking@fz-juelich.de, c.lerche@fz-juelich.de, n.j.shah@fz-juelich.de).

R. Trincheri and P. Cerello are with the Istituto Nazionale di Fisica Nucleare (INFN) Sezione di Torino, 10129 Torino, Italy (e-mail: riccardo.trincheri@to.infn.it, piergiorgio.cerello@to.infn.it).

Another issue creating specific requirements in shielding concepts is the amount of integration in MR-PET scanners. While in PET inserts for clinical MRI scanners for, e.g. brain imaging [15],[16], the amount of space for the PET ring components is comparably, whole-body MR-PET scanners aim for as much integration as possible for a compact design. This is driven by the fact that the already high price for a hybrid scanner can be reduced with a reduction of the bore size due to the domination of the magnet prices, which depend on the bore diameter. Furthermore, a compact PET ring close to the observation object increases PET scanner sensitivity and reduces the amount of required detectors due to the smaller diameter. It should be noted that a tight-fitting PET ring induces parallax errors if the depth-of-interaction problem is not solved [17]. Thus, in compact hybrid MR-PET scanner designs, the PET cassettes are located close to the image object. This implies that the shielding of the PET electronics is also located closer to the bore center. As a result, gradient-induced eddy currents more strongly affect the imaging region and spatial encoding inside the MRI field-of-view (FOV).

In MRI, RF coils, which include an RF screen, have faced the problem of induced eddy currents close to the observation object for years [18], [19]. There are several established methods of slitted designs to suppress gradient-induced eddy currents. However, an RF screen prevents a coil from coupling in the near field with its environment, protecting the coil from becoming detuned and unmatched. Moreover, radiation losses can be reduced. Here, the functionality of a very effective shield is not compromised and an attenuation of 15 – 20 dB is enough to prevent the coil from coupling strongly with the environment. On contrary, a PET cassette shielding should reduce interferences between PET electronics and RF coils completely. Adapted from an RF screen, the integration of a slitted shielding into a cylindric PET shielding was reported in [2]. Initial results of a first characterization of slitted shielding configurations were presented in [20].

In order to overcome previous limitations and restrictions, this work presents a gradient-transparent, frequency-selective shielding concept developed for the shield of the PET cassettes of hybrid MR-PET scanners located very close to the observation object. The shielding is characterized for an 1.5 T scanner, operating at 64 MHz. It provides high SE for  $B_1$ -fields at the Larmor frequency and a significant reduction of generated gradient eddy currents with respect to commonly used solid shielding configurations proposed for PET cassettes in MR-PET scanners. The frequency-selective behavior of the proposed shielding concept is characterized via both simulations and measurements, including MRI scans, and is compared to simulations and measurements of a solid shielding approach.

Moreover, this work demonstrates a method on how to design, tune and characterize a shielding for PET detector models with simulations and measurements. It also addresses potential problems with slitted shielding designs, which can be solved with a careful design of the shielding. Finally, simulation and measurement results explain where gradient-induced eddy currents occur and how they can be avoided.

## II. FREQUENCY-SELECTIVE SHIELDING CONCEPT

This section presents the frequency-selective shielding configurations proposed in this paper. In each case, the shield consists of a thin copper layer of 80–100  $\mu\text{m}$  thickness. The shield covers a plastic cassette of dimensions ( $69 \times 64 \times 412 \text{ mm}^3$ ) that acts as a mechanical support for the PET components. Dimensions were chosen for a typical brain scanner and insert cassettes as e.g. in [21].

In order to provide high attenuation of EM fields at the Larmor frequency, the thickness of the copper layer was chosen to be at least ten times the skin depth in copper at 64 MHz, to provide a high SE at RF [22]. The transparency to the gradients in the kHz range is obtained by interrupting the shield with thin slits ( $\leq 1 \text{ mm}$ ) placed parallel to  $B_0$ , as shown in Fig. 1.

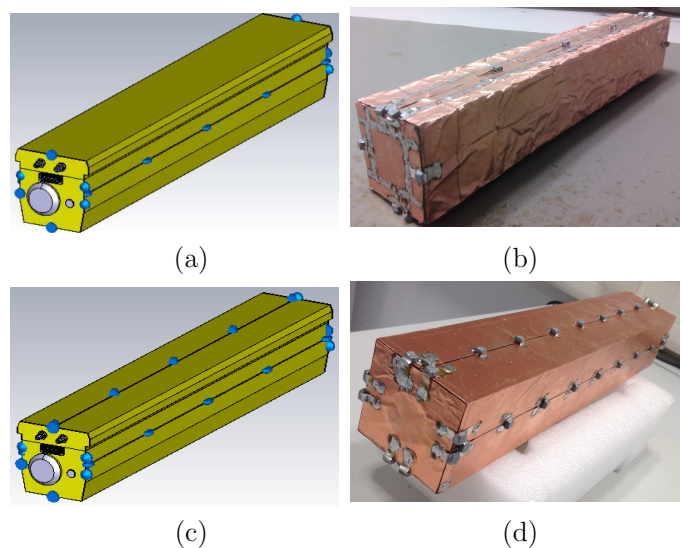


Figure 1. Model of the proposed frequency-selective shield implemented in the simulation setup with two slits on the left and right side (a), a prototype test cassette housing rotated by  $90^\circ$  resulting in 2 slits on top and bottom (b), model of the proposed frequency selective shield implemented with 4 slits parallel to  $B_0$  (c), and a prototype with 4 slits (d).

Found from first simulation results, the low-pass behavior for magnetic fields and thus the transparency of the shield for gradient fields was improved by means of additional slits close to the front and back sides of the cassette, where eddy currents are highest due to the effect of the longitudinal slits. Electrical continuity for the RF currents is guaranteed by a series of 10 nF non-magnetic capacitors, which are the blue dots in the simulation model in Fig. 1(a) and (c) and can also be seen on the first prototypes in Fig. 1(b) and (d). The interruptions and the capacitors provide a high impedance ( $> 10 \text{ k}\Omega$ ) for currents in the kHz range, to prevent low-frequency currents from flowing and enclosing the PET cassette, reducing the generation of scattered  $H$ -field polarized along the  $z$ -direction, which would interfere with gradient fields. On the other hand, for the high-frequency performance a continuous shielding is guaranteed via the capacitive bridges which presents a low ( $< 1 \Omega$ ) impedance in the MHz range.

In order to achieve a high SE for a frequency-selective cassette, compared to a continuous cassette shielding, the

proposed shield was optimized with EM simulation studies, which include effects from the geometry, other components (e.g. connectors), resonance phenomena and coupling through slits, holes and connectors. Especially where the slits along  $z$ -direction end in the slits on the front and backside of the cassette, coupling through the slits into the cassette was avoided with capacitive bridges to all 3 shield parts at this location because here coupling is more critical due to the connection of three slits.

### III. ANALYTICAL CONSIDERATION

The aim of this section is to provide a qualitative interpretation of the EM behavior of the proposed frequency-selective shield via an analytical formulation. It allows the estimation of the SE and the gradient distortion introduced by the shield at low-frequency and to better understand the physical phenomena behind these processes.

According to [23], at low-frequency the common solid shield can be approximated by the hollow shielding cylinder of infinite length shown in Fig. 2(a). The cylinder has an inner radius  $a$  and thickness  $t$  and is placed in a homogeneous magnetic field  $H_o$  along  $z$ -axis, while  $H_i$  is the magnetic field inside the shield.

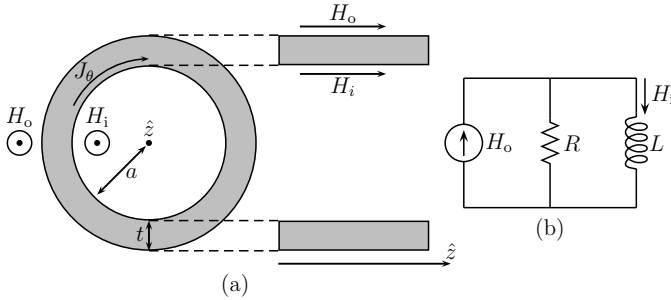


Figure 2. Model of a solid shielding approach. Here, the dashed lines connect between front and side view.

Begin by considering the following relations, derived from Maxwell's equations for highly conductive materials ( $\sigma \gg \omega\epsilon$ ) in [23]:

$$H_o - H_i = J_\theta(a)t = j\omega\mu_0\sigma\frac{at}{2}H_i, \quad (1)$$

where  $\omega = 2\pi f$  is the angular frequency,  $\mu_0$  is the magnetic permeability of the vacuum,  $\epsilon$  is the electrical permittivity of the metal,  $\sigma$  is the electrical conductivity of the metal and  $J_\theta$  represents the volume current density induced on the metal layer. The above equation is valid under the following assumptions:

- dimensions of the enclosure are much less than the free space wavelength
- very thin shield with respect to the skin depth  $t \ll \delta = 1/\sqrt{\pi f \mu \sigma}$

The SE for a magnetic field  $H$ , defined as  $SE_H$ , of the considered cylindrical structure can be easily derived from (1):

$$SE_{H,\text{solid}} = \frac{H_o}{H_i} = 1 + j\omega\mu\sigma\frac{at}{2}. \quad (2)$$

The circuitual interpretation of the above equation is presented in Fig. 2(b) where the magnetic field  $H_o$  is replaced by a current source, while the magnetic field inside the shield  $H_i$  is represented by the current, which flows through the inductor  $L$ . The element values are defined from (2) as  $R = \frac{2\pi a}{\sigma t}$  and  $L = \pi a^2 \mu_0$  representing the equivalent resistance and inductance per unit length [23].

From (1) and (2), it is clear that if there is no current flow  $J_\theta = 0$ , the magnetic field outside equals the magnetic field inside the shield  $H_o = H_i$ . This means that in this case the shield is transparent to the magnetic field leading to a  $SE_H = 1$  and to a reflected field of amplitude zero. It is important to note that for a solid shield the magnitude of both the  $SE_H$  and the reflected field grows linearly in frequency according to the induced current  $J_\theta$  and the metal conductivity  $\sigma$ .

In order to avoid a possible EM interaction with the MR environment, the low-frequency behavior of the shield must be emphasized to reduce the eddy-current generation and thus the scattered field during the gradient commutation and in the meanwhile providing a high  $SE_H$  at the Larmor frequency. The configuration presented in Sec. II can be used to improve the transparency achieved by the standard solid shield up to 1 MHz. The desired EM behavior is obtained from a solid configuration by opening a number of slits on the metal surface parallel to the incident fields  $H_o$  with a series of capacitor with value  $C_0$ , as shown in Fig. 3(a).

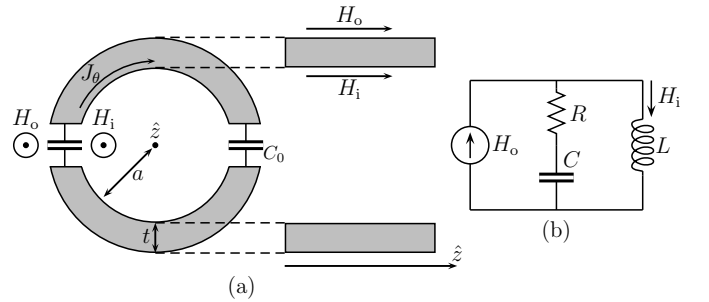


Figure 3. Model for estimating the effects of slits parallel to  $B_0$  and capacitive bridges. Here, the dashed lines connect between front and side view.

The circuit model in Fig. 3(b) allows one to approximate the effect of the capacitors and of the slits on the SE, which is obtained by connecting in series to the resistor  $R$  a capacitor  $C = 2C_0$  for the 2-slit version in order to achieve a frequency-dependent conductivity  $\sigma(\omega)$ . The model can be extended to more slits by adding more capacitors and therewith changing the equivalent capacitance  $C$ .

Under the previous assumptions,  $SE_H$  for the frequency-selective shield can be calculated as:

$$SE_{H,\text{disc}} = \frac{H_o}{H_i} = \frac{-\omega^2 LC + j\omega RC + 1}{1 + j\omega CR} \quad (3)$$

Equation (3) highlights the fact that the transparency of the shield to a low-frequency magnetic field is amplified by the pole  $p = -1/(RC)$  at frequency  $\omega_p = 1/(RC)$ , while at the high-frequency  $SE_{H,\text{disc}} \approx SE_{H,\text{solid}}$ .

The proposed simple analytical formulation is applied to estimate the SE of the solid and the frequency-selective

configuration of the copper shield in Fig. 5 for a linear polarized magnetic field along  $z$ . This kind of excitation will be introduced in the next section to mimic the effect of the shield on the gradient fields. According to [23] and Sec. II, the parameters in (2) for a generic shield are defined as follows:  $a = (2 \cdot 69 \cdot 64)/(69 + 62)$  mm (equivalent radius of a box with dimensions 69 mm $\times$ 62 mm),  $t = 80 \mu$ ,  $\sigma = \sigma_{Cu} = 5.96 \times 10^7$  S/m and  $C_0 = 10$  nF.

The proposed analytical model allows one to predict with a good accuracy the SE of the solid and frequency-selective shield up to 100 MHz. However, it is important to note that the model is accurate only in the bandwidth where the effect geometry of the shield (e.g., sharp edges, resonances, etc...) can be neglected.

#### IV. SHIELDING DESIGN

This section focuses on the design and the optimization of the proposed frequency-selective shielding based on simulation studies. In spite of its apparent simplicity, the RF shield is a critical component of a hybrid MR/PET scanner, since a design lacking care compromises the quality and the resolution of the MRI images, as will be demonstrated in section V, and can lead to additional  $\gamma$ -ray attenuation. For this reason, the design and the characterization of the proposed shielding concept was carried out carefully and systematically via set of time- and frequency-domain simulations, respectively.

The final version of the proposed shield was developed via an iterative process, based on a large number of EM simulations with the aim of finding the best configuration in terms of copper thickness, values and positions of the capacitors, and number and position of the slits. Obviously, the number of simulations was limited by simulation time, which can be very long since RF and gradient fields must be included in the simulation framework. The simulation time was reduced replacing the MR fields by several plane wave excitations with different polarizations [24]. During the design phase the latter approximation allowed one to test for a large number of different shielding configurations and to better understand the behavior of the eddy current induced on the shield during the gradient switching. In particular, the EM interaction between the shield and the MR fields was characterized by means of numerical simulations in frequency- and time-domain in CST MICROWAVE STUDIO via the 3D model of the cassette of Fig. 1(a) and (c) [25].

It should be mentioned that typically required openings in the shielding as holes for connectors, cooling pipes, etc..., cf. Fig. 1(a) and (c), are integrated into the simulations, as they are part of the shielding and influence the SE and shielding behavior.

##### A. Frequency-Domain Simulations

The SE for both the  $B_1$ - and the gradient fields were calculated from the simulation results by considering the  $H$ -field inside the shield for a circularly and linearly polarized incident plane wave respectively, as shown in the simulation setup in Fig. 4.

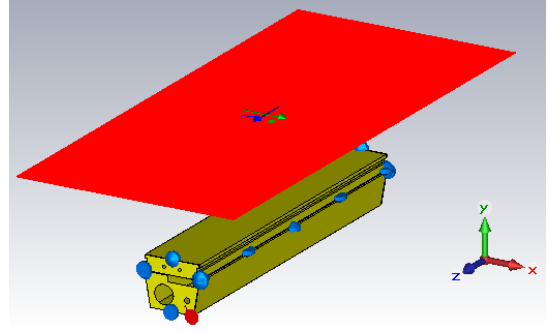


Figure 4. Simulation setup for the estimation of the SE and the gradient perturbations. The red area represents the incident plane wave.

The  $B_1$ -field of the MR was modeled as a circularly polarized EM plane wave rotating in the  $xy$ -plane [26], while the gradient fields were described by linearly polarized plane waves with the magnetic field  $H$  along the  $z$ -axis. In Fig. 5, the resulting SE values of the proposed frequency-selective shielding configuration are compared with a standard solid shield. The plot also includes the calculated SE from the model derived in section III.

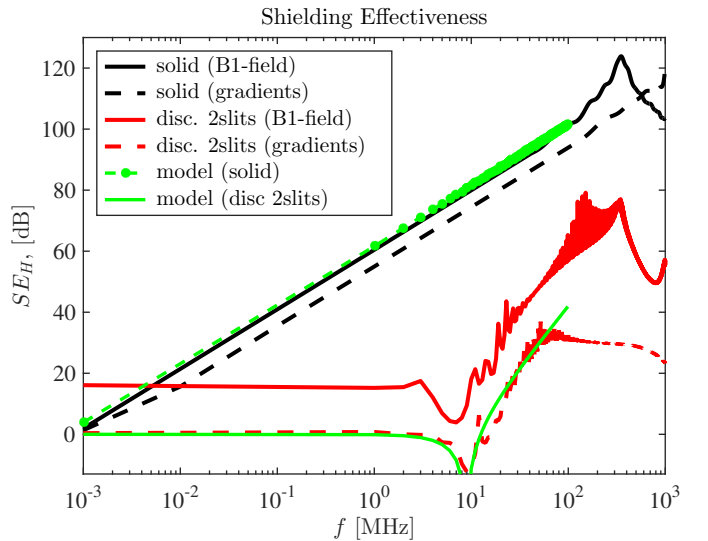


Figure 5. SE of the solid (black lines) and the proposed frequency selective (red curves) shields for the  $B_1$ - (solid lines) and the gradient (dashed lines) fields obtained via frequency-domain simulations. The simulated results are compared to the SE calculated with the model in section III represented by the green curves.

According to simulation results, the proposed solution with 2 slits has a SE of 64.17 dB at the Larmor frequency of 64 MHz, providing a high protection to the PET electronics, similar to the solid shield. The SE of a cassette with 4 slits is 62.5 dB at 64 MHz providing a similar high SE as the 2-slit version. The main difference between the solid and the frequency-selective shields is in the frequency bandwidth below 10 MHz, where the proposed configuration provides a high transparency to gradient fields and therefore has a  $SE \approx 0$  dB. The transparency to the gradient fields is also investigated in Fig. 6 by calculating the perturbation of the magnetic field introduced by the metal shield in the FOV

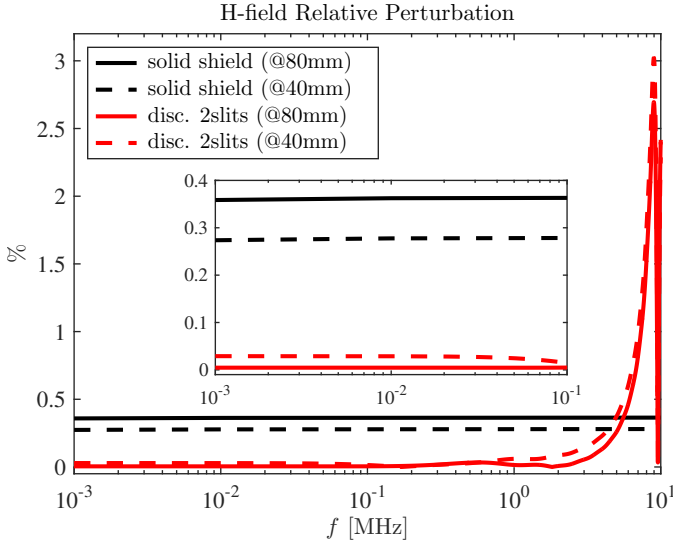


Figure 6. Relative gradient fields perturbation in the frequency-domain for the solid (black curves) and the proposed frequency-selective shield (red curves) for different positions in the FOV.

at a distance of 40 mm and 80 mm from the center of the cassette for a linearly polarized plane wave with the  $H$ -field along the  $z$ -direction. According to the curves shown in Fig. 6, the perturbation introduced by the solid configuration is almost constant in the frequency bandwidth from 1 kHz to 10 MHz, whereas the behavior of the proposed frequency-selective shield depends on the excitation frequency and on the polarization of the incident  $H$ -field. Here, the differences between a 2-slit and 4-slit version cannot be distinguished in the simulations due to the accuracy of the simulation setup and the fact that a 2 slit-shielding configuration already provides a significant reduction of the gradient perturbations.

A more intuitive description of the previous results is provided by the field maps in Fig. 7, which compare the  $H$ -field maps for a standard shield and the proposed solution with 2 slits by considering linearly-polarized plane waves at two different frequencies. Comparing Fig. 7(b1) with Fig. 7(a1), it is clear that the frequency-selective shield is almost transparent to a low-frequency excitation at 10 kHz, while it demonstrates a high SE for 64 MHz excitation, protecting the PET electronics inside the cassette as shown in Fig.7(b2), as given for the solid cassette shielding in Fig.7(b1).

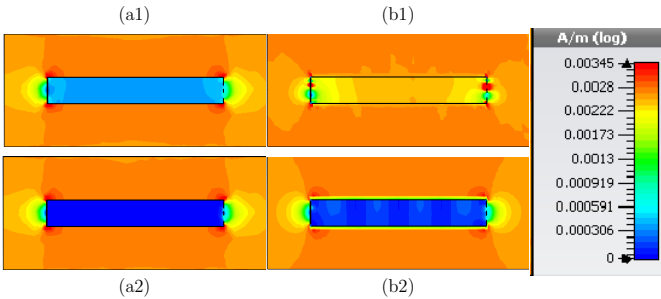


Figure 7.  $H$ -field maps for the solid (left side, (a)) and the frequency-selective (right side, (b)) shield for excitations induced by a 10 kHz (upper pictures, (1)) or a 64 MHz (bottom pictures, (2)) plane wave.

## B. Sensitivity Analysis

A sensitivity analysis was performed on both, the solid and the frequency-selective shields, in order to understand their robustness in presence of an uncertainty/tolerance on the thickness of the copper layer caused by the manufacturing process.

Table I  
RESULTS OF THE SENSITIVITY ANALYSIS FOR DIFFERENT SHIELD THICKNESSES.

Shielding Configuration	Metal Thickness	SE <sub>H,RF</sub> @64 MHz	Gradient Perturbation in FOV		
			40 mm	80 mm	128 mm
Solid	80 $\mu\text{m}$	96.54 dB	0.36 %	0.28 %	0.07 %
	100 $\mu\text{m}$	98.57 dB	0.36 %	0.28 %	0.08 %
	500 $\mu\text{m}$	112.10 dB	0.37 %	0.29 %	0.08 %
Discontinuous (2 slits)	80 $\mu\text{m}$	66.51 dB	0.03 %	0.05 %	0.07 %
	100 $\mu\text{m}$	69.23 dB	0.03 %	0.06 %	0.07 %
	500 $\mu\text{m}$	65.53 dB	0.09 %	0.06 %	0.06 %

In particular, Table I collects the simulation results of the SE and the gradient perturbations at three different positions in the FOV, defined as the distances from the center of the cassette for different thicknesses and configurations of the shield. The proposed solution clearly reduces the gradient perturbation in the FOV region close to the shield, providing a high SE for the  $B_1$ -field. In addition, the results of the sensitivity analysis show that the gradient perturbations and the SE of the considered shielding scheme are independent of a possible non-uniformity in the thickness of the shield metal layer. In fact, both the electrical conductivity and the SE of the discontinuous shield are dominated by the behavior of the capacitors.

## C. Time-Domain Simulations

The effect of the shield on the gradient fields was investigated via low-frequency time-domain simulations. The solid and the discontinuous shields were inserted in a switched  $H$ -field with a gradient along  $z$  simulated as a Helmholtz coil driven with currents flowing in opposite directions, as shown in Fig. 8. Due to the simplicities of modeling  $z$ -gradients with a Helmholtz coil, whereas for  $x$ - and  $y$ -gradients another coil setup is required, effects of  $x$ - and  $y$ -gradients are studied in detail experimentally in section V.

The gradient field along  $z$ -axis is obtained by using two coils in a complementary supply condition which are switched on and off periodically with a 1 kHz square wave excitation with a slew rate of 50  $\mu\text{s}$ . The results in Fig. 9 for the 2-slit and the 4-slit cassette version enable the comparison of the effect of the induced eddy-current during gradient switching for the solid and the frequency-selective shielding configurations. It demonstrates that the gradient field disturbances arising from gradient switching are significantly higher for solid cassette shielding compared to the proposed interrupted shields.

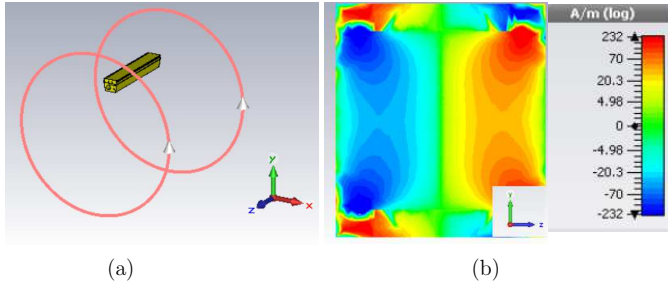


Figure 8. Panel (a): simulation setup for a time-domain gradient simulation consisting of the shielded cassette and of two Helmholtz coils. Panel (b): field map of the amplitude of the gradient field excitation considered in the simulation.

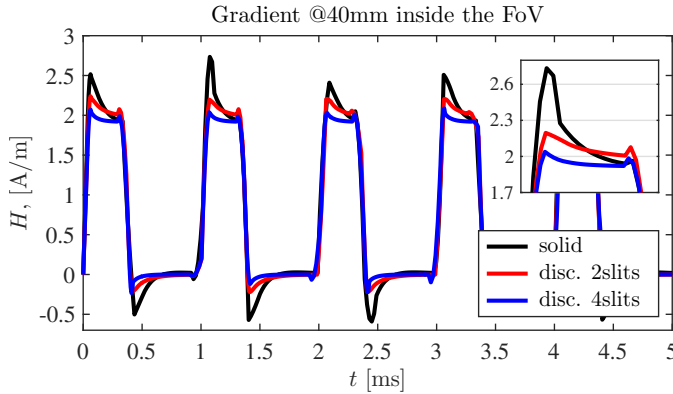


Figure 9. H-field at a distance of 40 mm from the center of the shield computed for the solid (black curve) and the proposed discontinuous shields with 2 slits (red curve) and 4 slits (blue curve), respectively.

## V. EXPERIMENTAL VALIDATIONS

The simulation results were validated via measurements. Prototypes of both the solid and of the frequency-selective shields were built and characterized via SE bench measurements and MR images. The evaluated prototypes of the frequency-selective shielding consist of a version with 2 slits and 4 slits, as shown in Fig. 1(b) and (d). Moreover, effects depending on the gradient orientation were studied.

### A. Shielding Effectiveness

The measurement setup for the SE determination of Fig. 10 consisted of a MR surface coil built in-house and a pick-up loop antenna placed outside and inside the shield and connected to the ports of a vector network analyzer. The MR surface coil was carefully tuned and matched to the Larmor frequency and PET cassette environment. The SE at the Larmor frequency of 64 MHz was measured on a metal-free table via a set of 2-port scattering measurements considering the solid and both discontinuous shield configurations. A reference measurement without a cassette was performed. For each measurement of each prototype and for the reference measurement, the coil was tuned and matched to achieve the same conditions. Table II compares the measured to the simulated SE of a solid shield with the proposed low-pass shields.

A  $SE_H = 57.19$  dB for the prototype with 2 slits parallel to  $B_0$  and  $SE_H = 50.13$  dB for the version with 4 slits was



Figure 10. Measurement setup with PET cassette prototypes and an MR surface coil tuned to the cassette environment at 64 MHz.

Table II  
COMPARISON BETWEEN THE MAIN FIGURES OF MERIT FOR THE SOLID AND DISCONTINUOUS SHIELDING CONFIGURATIONS.

Shielding Conf.	$SE_{H,RF}@64$ MHz	
	Simulation	Measurement
Solid	95.81 dB	69.23 dB
Disc. (2 slits)	64.17 dB	57.19 dB
Disc. (4 slits)	62.5 dB	50.13 dB

achieved with the proposed designs; for comparison  $SE_H = 69.23$  dB was achieved for the solid shield. The differences between the simulation results and the measurements for the solid configuration are due to possible EM leakage in the shield (e.g., small holes, defects in the metal layer) or to a coupling of the pick-up loop antenna with the metal shield that cannot be unequivocally included in the simulation environment.

### B. Gradient Dependencies

To evaluate gradient transparency, the measurement setup was extended with an MR proton phantom covering the coil FOV, as shown in Fig. 11. The distance between the cassette housing and RF coil was 2 cm. The distance between the RF coil and phantom was also assembled to be 2 cm, resulting in a minimal distance of 4 cm between copper surface of the cassette and phantom. Since gradient distortions are independent of the Larmor frequency, the setup was evaluated in a home-assembled 4 T MRI human scanner based around a Siemens console with a second RF surface coil built in-house and tuned and matched to 168 MHz. Measurements were taken with different shields to compare the solid and the frequency-selective designs. Before each measurement, the MR coil was carefully tuned to the Larmor frequency and matched to the new environment to compensate for the detuning and dematching introduced by the shield configurations. Moreover, a reference measurement without any cassette was considered. EPI sequences (TE 30 ms, TR 500 ms) were applied with different bandwidths resulting in echo spacing times between 0.3 and 0.88 ms, cf. Fig. 16. Slice selection was applied along  $B_0$ -direction defined as  $z$ -direction. Phase encoding direction was changed between  $x$ - and  $y$ -directions, defining  $x$ -direction as the direction pointing from the most right point of the scanner bore to the most left point and  $y$ -direction as the direction between most bottom to most top point of the scanner bore. The cassette position inside the scanner bore was also changed to acquire images for different cassette positions of a PET ring.



Figure 11. Measurement setup used to evaluate the effect of the shield on EPI images. All the images of the cassettes with the solid and the slitted shields were acquired at 4T.

The resulting images measured without a cassette (reference image) and a solid prototype cassette are shown in Fig. 12. The EPI image of the phantom without the shielded PET cassette in Fig. 12(a) shows the typical FOV of a surface coil on the cylindrical phantom and no disturbances as gradient eddy current artifacts. Gradient induced eddy current artifacts occur as black stripes with signal drop offs in Fig. 12(b) in scans of the phantom together with the solid prototype cassette.

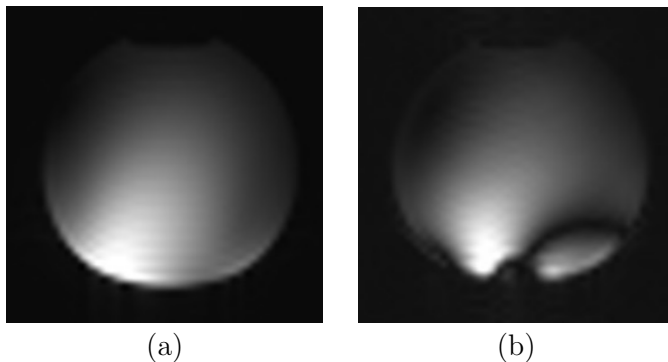


Figure 12. EPI images acquired as a reference image with no PET cassette in the measurement setup (a) and EPI images with gradient eddy current artifacts in the present of a cassette with a solid shield (b).

EPI images acquired with the prototype cassette with 2 slits measured for different orientations of the whole measurement setup as well as different phase encoding directions, are depicted in Fig. 13. For this cassette, one slit is located at each surface of the cassette oriented along  $yz$ -direction in the non-rotated setup, which result in the exact configuration as photographed in Fig. 11. In Fig. 13(a) and (b), as can be identified on the FOV of the RF coil, the PET cassette and surface coil are placed below the phantom. The phase encoding direction in Fig. 13 (a) was set to anterior to posterior (A>P) and in Fig. 13(b) it was encoded from right to left side (R>L). In case of A>P direction, no measurable eddy current artifacts occur while the EPI image with phase encoding direction of R>L shows artifacts similar to a cassette with a solid shield. Images acquired with a setup rotated by  $90^\circ$  resulting in an RF coil and PET cassette on the left side are given in Fig. 13(c) and (d). Phase encoding direction in Fig. 13(c) was chosen to A>P direction as well as to R>L direction in Fig. 13(d).

Eddy current artifacts occur in the image of Fig. 13(c), no measurable artifacts occur in the image of Fig. 13(d).

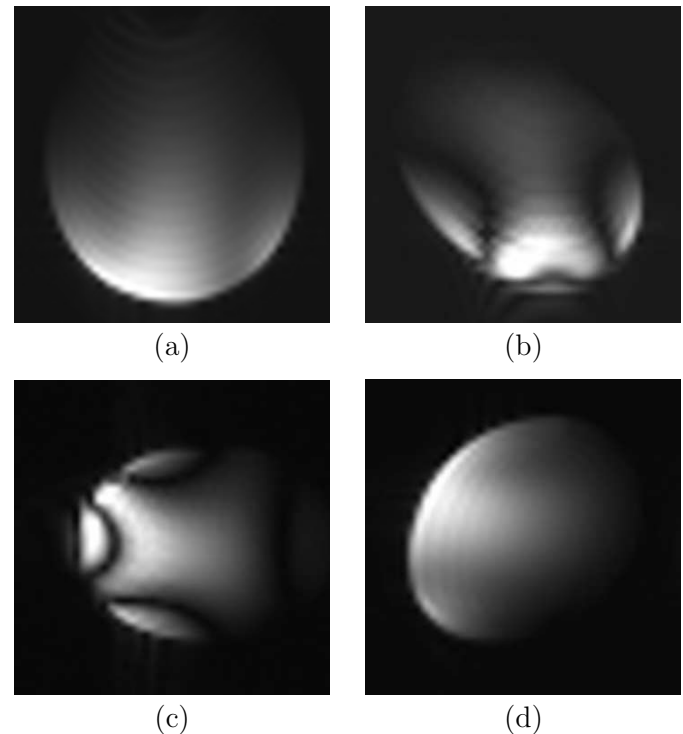


Figure 13. EPI images of the prototype cassette with 2 slits, one at each  $yz$ -oriented surface of the cassette in the non-rotated setup. Although not visible, the RF coil and the PET cassette are at the bottom of the image (a) and (b) and on the left side in image (c) and (d). Phase encoding direction was set to A>P in image (a) and (c) and to R>L in image (b) and (d).

Moreover, the same EPI images were acquired for a setup, where the two slits of the prototype cassette are assembled in the surface of the PET cassette next to the RF coil and on the opposite side. Hence, in the non-rotated setup the slits are in the  $xz$ -oriented surfaces of the cassette. This setup is equal to the photographed setup in Fig. 11 with a rotation of only the PET cassette by  $90^\circ$  without rotating the whole setup. The resulting EPI images are shown in Fig. 14. An EPI image with the RF coil and PET cassette located on the bottom of the image is shown in Fig. 14(a). There, eddy current effects occur. The resulting images of the setup rotated by  $90^\circ$  is given in Fig. 14(b) and (c). The coil and cassette are placed there in the left side of the image resulting in no artifact for A>P phase encoding direction (b) and in eddy current artifacts for a R>L phase encoding direction (c). Fig. 14(d) shows the setup rotated only by  $45^\circ$  instead of  $90^\circ$ . In this case artifacts due to gradient eddy currents on the PET cassette occur for both the selected phase encoding directions.

In addition to the 2-slit prototype cassette, the prototype with 4 slits, one on each cassette side along  $z$ , as shown in Fig. 1(d), was also evaluated with a series of EPI sequence scans. As shown in Fig. 15, independent from measurement setup orientation ( $0^\circ$  and  $90^\circ$  rotations) and the phase encoding direction (A>P and R>L), the images are free of gradient eddy currents artifacts. Here, Fig. 15(a) and (b) show acquired EPI images where the RF coil and PET cassette prototype are

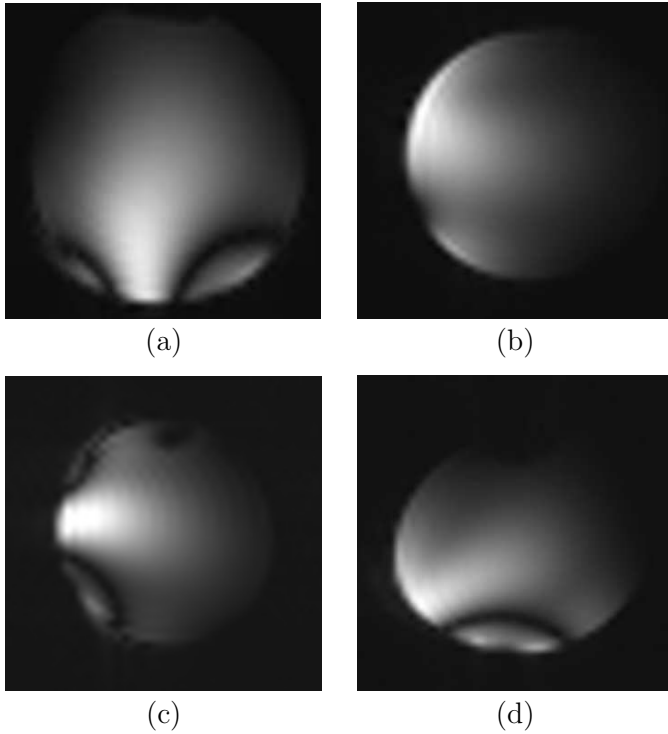


Figure 14. EPI images of the prototype cassette with 2 slits at the side next to the surface coil and its opposite side. Although not visible, the RF coil and the PET cassette are at the bottom of the image (a) and on the left side in image (b) and (c). RF coil and PET cassette are placed on the left bottom corner of the image (d). Phase encoding direction was set to A>P in image (a), (b) and (d) and to R>L in image (c).

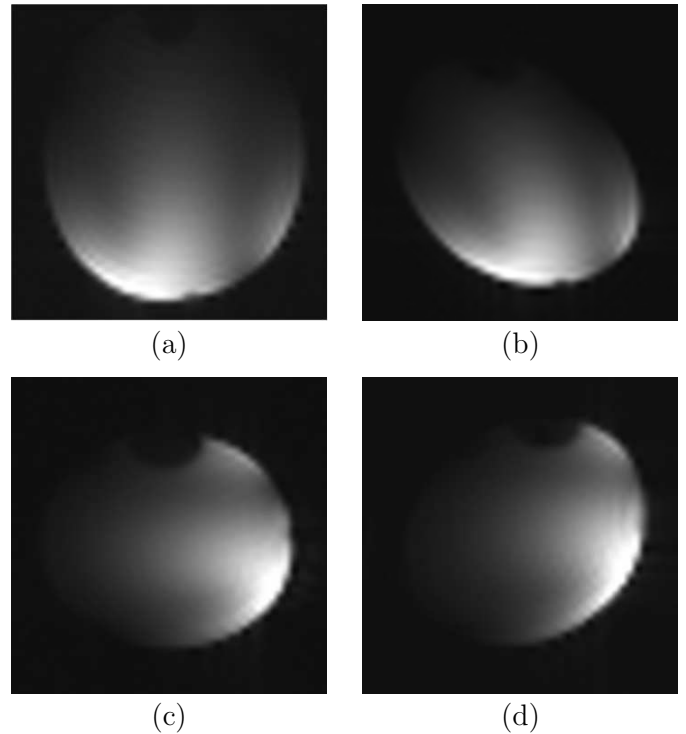


Figure 15. EPI images of the prototype cassette with 4 slits. Although not visible, the RF coil and the PET cassette are at the bottom of the image (a) and (b) and on the right side in image (c) and (d). Phase encoding direction was set to A>P in image (a) and (c) and to R>L in image (b) and (d). The black holes on top of the images are caused by air inside the phantom.

placed on the bottom of the phantom. Fig. 15(c) and (d) are scanned with the RF coil and cassette placed on the right side of the phantom. The phase encoding direction of the EPI sequence was selected to A>P direction in Fig. 15(a) and (c) and to R>L in Fig. 15(b) and (d).

## VI. DISCUSSIONS AND DESIGN CONSIDERATIONS

### A. Shielding Effectiveness

The proposed gradient-transparent shielding designs, consisting of slits interrupting gradient eddy currents flowing perpendicular to the slit directions and capacitive bridges ensuring high frequency currents to pass through guaranteeing a continuous shielding with strong SE, demonstrate a high SE in the MHz range with more than 50 dB attenuation. Here, simulation and measurement results determine slightly different results for the SE in the MHz range. This is especially the case for the solid version, which is due to an imperfect measurement, because the pickup loop inside the cassette has to be connected to the network analyzer port outside the cassette. As evaluated in the simulation and measurement results, the SE compared to a solid shielding is slightly reduced by integrating slits and by increasing the number of slits. As a consequence, an integration of more than 4 slits is not recommended to ensure a SE higher than 50 dB. The SE also depends on the number of capacitive bridges. By adding more capacitors one reduces SE losses significantly, especially when decreasing the distances between capacitive bridges along long

slits. It should be mentioned that this design is proposed for 1.5 T scanners. RF coupling through the slits is increased for higher frequencies, that is, for scanners with a  $B_0$  field strength higher than 1.5 T.

Due to the present of capacitors in the proposed concept, the common problem of RF closed housings can be solved. Capacitive bridges can be used to close slits which are a result of openings in the housing to enable access to the PET electronic. Instead of, e.g., soldering the lid of the shield required for opening the cassette or installing conductive seals between lid and the rest of the cassette, the capacitors can be soldered and desoldered when opening/closing the cassette. Depending on cassette design, this can accelerate the process of gaining access to the inside of the cassette. On the other hand, solder of capacitors inside the FOV of the PET ring induces a problem of attenuation of the  $\gamma$ -rays which should ideally be avoided.

### B. Gradient Induced Eddy Currents

The main focus of this work is to reduce eddy currents induced by very fast gradient switching times while providing a high SE in the MHz range. The results of this work demonstrate that the cassette shielding design significantly influences gradient induced eddy current artifacts. Therefore, the MRI image quality in hybrid MR/PET scanners is expected to be increased if the proposed shielding concept is applied.

The derived analytical solution and the frequency domain simulations demonstrate the transparency of the shield in

the kHz range for linearly polarized EM waves with the magnetic component along  $z$ -direction. To include gradient fields, time domain simulations describing a magnetic field  $G_z \cdot z$  pointing in  $z$ -direction with a gradient along  $z$  were used. The simulation results demonstrate decreased disturbed magnetic fields due to the proposed concepts with 2 and 4 slits compared to solid shielding. The time domain simulations have the advantage of enabling quantitative estimation of  $G_z$  artifacts of different simulated cassettes. The model is limited by two aspects. First, due to its simplicity,  $z$  gradients are included, though no  $x$  and  $y$  gradients can be included without developing a more complex model. Second, the Helmholtz coil is a simple coil to produce a magnetic gradient field. MRI scanners include more complexed gradient systems, which are being continuously optimized [27]. Furthermore, novel gradient coil concepts, specialized for MR-PET scanners, are being developed [28].

To provide a complete characterization of the proposed shielding concept, empiric EPI scans are included in this study. The measurement results from a human 4T scanner include effects from real coils generating magnetic fields pointing in  $z$  direction with a linear magnitude variation along  $x$  and  $y$  direction. The acquired images demonstrate that not only the cassette surfaces oriented along  $xz$ -direction effects eddy current artifacts, but also the surfaces along  $yz$ -direction, with respect to Fig. 11. This is an important fact which has to be considered in PET cassette shielding designs and this problem is not given in RF screen designs for MRI coil and in [2]. In addition, the eddy current effects are strongly depending on the selected phase encoding direction in the tested EPI sequence.

Fig. 16 shows the sequence diagram of an EPI sequence. For the measurements in this study, as mentioned before, slice selection was chosen only along  $z$  direction. As a consequence, the slice selection gradient in Fig. 16 is equal to physical gradient  $G_z$  of the MRI scanner. Moreover, phase and frequency encoding gradients can be replaced by the physical gradients  $G_x$  and  $G_y$ , where one physical gradient is only contributing to phase or frequency encoding in the applied experiments. Considering a magnetic field, applied by all gradient coils, the total field results in a magnetic field given by  $(G_x \cdot x + G_y \cdot y + G_z \cdot z)\vec{e}_z$ . Eddy current influences from  $G_z$  can be ignored in EPI sequences because the full  $k$ -space of a slice is acquired with a single excitation field, which means that the slice selective gradient  $G_z$  is switched only once. In EPI sequences the phase encoding gradient is significantly lower than the frequency encoding gradient, as shown in Fig. 16, because with the phase encoding gradient only the next  $k$ -space line is addressed, which can be realized with low gradient amplitudes. Hence, depending on the chosen phase encoding direction in the EPI sequence, that is, either the  $x$ - or  $y$ -direction,  $G_x$  or  $G_y$  gradients should not have a significant influence on eddy currents. Moreover, results from section V-B demonstrate that for the 2-slit version of the cassette the orientation of the phase encoding direction resp. frequency encoding direction relative to the orientation of the slitted and unslitted surfaces influences the appearance of eddy current artifact. Defining the A»P direction inside the bore as  $y$ -direction and the R»L phase encoding direction as  $x$ -

direction, and selecting an A»P phase encoding direction in the sequence parameters, the measurements demonstrate that eddy currents artifacts only occur if the cassette surfaces, oriented along  $y$  direction, are not interrupted by slits. This means that gradient eddy currents on the surfaces perpendicular to the frequency encoding direction lead to the observed artifacts of Fig. 12–15. As a consequence, in EPI sequences artifacts can be suppressed by reducing eddy currents on the surfaces perpendicular to the frequency encoding direction by adding slits parallel to  $z$  direction into these cassette surfaces.

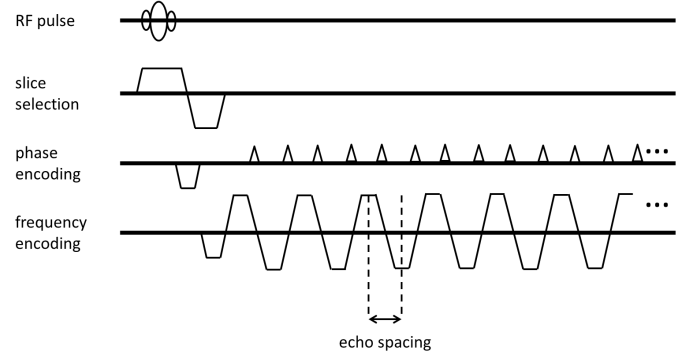


Figure 16. Sequence diagram of an EPI sequence showing the behavior of slice selection, phase encoding and frequency encoding gradients.

In practice, the slice-selection direction can be chosen by the scanner operator to be in any oblique or double oblique direction. This results in phase encoding directions with mixed  $x$  and  $y$  components. This consideration indicates that the 4-slit version is the design of choice to reduce all gradient artifacts, because gradient induced eddy currents are reduced on all 4 large surfaces of the cassette, while still providing a high SE. It should be mentioned that eddy currents flowing in  $z$  direction will generate magnetic fields without  $z$  component and therefore will not interfere with the gradient fields. It should also be mentioned that for very compact hybrid MR-PET scanners, the PET cassettes can be located very close to gradient coils and hence outside the MRI FOV, which results in  $\vec{e}_x$  and  $\vec{e}_y$  magnetic field components of the gradient coils. For higher frequencies and MRI magnets with higher field strengths, especially for ultra-high field MRI, RF coupling through the slits becomes a more critical aspect with respect to the SE. This problem can be solved by adding more capacitors to the slits resulting in smaller distances between the capacitors.

## VII. CONCLUSIONS

According to the previous sections, the proposed frequency-selective shield was optimized in order to provide a high SE at the Larmor frequency ( $>50$  dB (measured)). This means that the shield attenuates the B1 field of a factor  $> 300$ , avoiding possible noise interferences with the PET electronics. On the other hand, it clearly reduces the gradient field distortion, minimizing the eddy current generation on all metal surfaces of the shield during the gradient switching with respect to the standard solid shield. In addition, the results of the sensitivity

analysis show that the considered shielding scheme is independent of a possible non-uniformity in the thickness of the shield metal layer. This aspect is very important, especially from a practical point of view, since it simplifies shield construction. The results confirm the feasibility and the strength of the proposed solution, as well as its advantages with respect to a standard approach.

Furthermore, the methodology and the simulation environment presented in this work can be easily extended for the characterization of other components as cooling systems, electronic boards, connectors and cables etc. to understand their influences on the MR compatibility aspects in more detail. In addition to the inclusion of other components, further work can extend the simulation model with  $x$  and  $y$  gradient coils. This will result in additional time domain simulation results, including eddy currents and magnetic field changes due to  $G_x$  and  $G_y$  gradients.

### VIII. ACKNOWLEDGMENT

The research leading to these results has received part funding from the European Union Seventh Framework Program (FP7 2007-2013) under Grant Agreement No. 602621-TRIMAGE.

The authors would like to thank their colleagues Mr. Vlad Badiu and their project partners from TRIMAGE.

### REFERENCES

- [1] Y. Shao, *et al.*, “Development of a PET detector system compatible with MRI/NMR systems”, *IEEE Trans. Nucl. Sci.*, vol. 44, issue 3, pp. 1167–1171, Jun. 1997.
- [2] B. Pichler, *et al.*, “Performance test of an LSO-APD detector in a 7-T MRI scanner for simultaneous PET/MRI”, *J. Nucl. Med.*, vol. 47, no. 4, pp. 639–647, Apr. 2006.
- [3] D. P. McElroy, V. Saveliev, A. Reznik, and J. A. Rowlands, “Evaluation of silicon photomultipliers: A promising new detector for MR compatible PET”, *Nuclear Instruments and Methods in Physics Research A*, vol. 571, issue 1–2, pp. 106–109, Feb. 2007.
- [4] C. Piemonte, *et al.*, “Characterization of the First Prototypes of Silicon Photomultiplier Fabricated at ITC-irst”, *IEEE Trans. Nucl. Sci.*, vol. 54, issue 1, pp. 236–244, Feb. 2007.
- [5] A. Berneking, “Characterization of Sensitivity encoded Silicon Photomultiplier for high resolution simultaneous PET/MR Imaging”, Diploma thesis, Faculty of Electrical Engineering and Information Technology, RWTH Aachen, Aachen, Germany, 2012.
- [6] A. Berneking, A. Gola, N. J. Shah, and C. W. Lerche, “A New DOI PET Detector Concept for Linearly Graded Silicon Photomultiplier in Hybrid MR/PET”, presented at the PSMR conference, Cologne, Germany, May 23–25, 2016.
- [7] J. C. Zhang, L. Cai, J. H. Wang, Z. M. Shen, F. K. Tang, and L. J. Meng, “A dual-mode readout system for a MR-Compatible ultrahigh resolution SPECT/PET system”, *IEEE Nuclear Science Symposium and Medical Imaging Conference (NSS/MIC)*, pp. 4196–4198, Nov. 2012.
- [8] B. Weissler, *et al.*, “MR compatibility aspects of a silicon photomultiplier-based PET/RF insert with integrated digitisation”, *Phys. Med. Biol.*, vol. 59, no. 17, Aug. 2014.
- [9] C. Levin, T. Deller, W. Peterson, S. H. Maramraju, C. Kim, and R. Prost, “Initial results of simultaneous whole-body ToF PET/MR”, *J Nucl Med.*, vol. 55, no. 660, May 2014.
- [10] S. H. Maramraju, *et al.*, “Electromagnetic Interactions in a Shielded PET/MRI System for Simultaneous PET/MR Imaging in 9.4 T: Evaluation and Results”, *IEEE Trans. Nucl. Sci.*, vol. 59, no. 5, pp. 1892–1899, Oct. 2012.
- [11] S. Geetha, K. K. S. Kumar, C. R. K. Rao, M. Vijayan, and D. C. Trivedi, “EMI shielding: Methods and materials—A review”, *Journal of Applied Polymer Science*, vol. 112, issue 4, pp. 2073–2086, May 2009.
- [12] M. K. Stehling, R. Turner, and P. Mansfield, “Echo-planar imaging: magnetic resonance imaging in a fraction of a second”, *Science*, vol. 254, Issue 5028, pp. 43–50, Oct. 1991.
- [13] M. Zaitsev, K. Zilles, and N. J. Shah, “Shared k-space echo planar imaging with keyhole”, *Magnetic Resonance in Medicine*, vol. 45, issue 1, pp. 109–117, Jan. 2001.
- [14] S. Y. Huang, *et al.*, “The impact of gradient strength on in vivo diffusion MRI estimates of axon diameter”, *NeuroImage*, vol. 106, pp. 464–472, Feb. 2015.
- [15] H.-P. W. Schlemmer, *et al.*, “Simultaneous MR/PET Imaging of the Human Brain: Feasibility Study”, *RSNA Radiology*, vol. 248, issue 3, Sep. 2008.
- [16] H. Herzog, *et al.*, “High resolution BrainPET combined with simultaneous MRI”, *Nuklearmedizin*, vol. 50, pp.74–82, Feb. 2011.
- [17] C. Lerche, *et al.*, “Depth of interaction detection for  $\gamma$ -ray imaging”, *Nucl. Instr. and Meth. A*, vol. 600, pp.624–634, Feb. 2008.
- [18] J. Chen, Z. Feng, and J. M. Jin, “Numerical simulation of SAR and B1-field inhomogeneity of shielded RF coils loaded with the human head”, *IEEE Trans. on Biomed. Eng.*, vol. 45, issue 5, pp. 650–659, May 1998.
- [19] M. Alecci, and P. Jezzard, “Characterization and Reduction of Gradient-Induced Eddy Currents in the RF Shield of a TEM Resonator”, *Magn Reson Med.*, vol. 48, issue 2, pp. 404–407, Aug. 2002.
- [20] A. Berneking, R. Trinchero, N. J. Shah, P. Cerello, and C. W. Lerche, “Design and Characterization of a Frequency Selective RF Shield for PET Detector Modules in Hybrid MR-PET Imaging”, presented at the PSMR conference, Cologne, Germany, May 23–25, 2016.
- [21] H. Herzog, U. Pietrzyk, N. J. Shah, and K. Ziemons, “The current state, challenges and perspectives of MR-PET”, *NeuroImage*, vol. 49, issue 3, pp.2072–2082, Feb. 2010.
- [22] C. R. Paul, *Introduction to Electromagnetic Compatibility*, 1992, Wiley-Interscience.
- [23] W. W. Cooley, “Low-Frequency Shielding Effectiveness of Nonuniform Enclosures”, in *IEEE Trans. Electromagn. Compat.*, vol. 10, pp. 34–43, March 1968.
- [24] R. H. Caverly, “MRI Fundamentals: RF Aspects of Magnetic Resonance Imaging (MRI)”, *IEEE Microw. Mag.*, vol. 16, no. 6, pp. 20–33, July 2015.
- [25] T. Weiland, M. Timm, and I. Munteanu, “A practical guide to 3-D simulation”, *IEEE Microw. Mag.*, vol. 9, no. 6, pp. 62–75, Dec. 2008.
- [26] J. G. Sled, and G. B. Pike, “Standing-wave and RF penetration artifacts caused by elliptic geometry: an electrodynamic analysis of MRI”, *IEEE Trans. on Med. Imag.*, vol. 17, issue 4, pp. 653–662, Aug. 1998.
- [27] M. Poole, and R. Bowtell, “Novel gradient coils designed using a boundary element method”, *Concepts in Magnetic Resonance Part B: Magnetic Resonance Engineering*, vol. 31B, issue 3, pp. 162–175, Aug. 2007.
- [28] M. Poole, *et al.*, “Split gradient coils for simultaneous PET-MRI”, *Magnetic Resonance in Medicine*, vol. 62, issue 5, pp. 1106–1111, Nov. 2009.